Journal of Materials Chemistry A

ROYAL SOCIETY OF CHEMISTRY

PAPER

View Article Online
View Journal | View Issue

Cite this: J. Mater. Chem. A, 2023, 11, 1199

A chemically bonded and plasmonic Z-scheme junction for high-performance artificial photosynthesis of hydrogen peroxide†

Teng Shao,‡[a] Yuan Chang,‡[b] Zhuwei Li,[a] Yurou Song,[a] Dingfeng Jin,[a] Junfeng Gao,[b] Licheng Sun[cde] and Jungang Hou*[a]

Received 23rd November 2022
Accepted 15th December 2022

DOI: 10.1039/d2ta09122d

rsc.li/materials-a

Artificial photosynthesis has been regarded as a promising solution for the clean, sustainable, and efficient production of hydrogen peroxide (H_2O_2). However, rigorous regulation of light absorption, charge transfer, and surface kinetics is significant for catalytic performance. As a proof of concept, we report a chemically bonded and plasmonic Z-scheme junction as a model material prepared by the *in situ* assembly of nonstoichiometric $W_{18}O_{49}$ (WO) onto two-dimensional carbon nitride nanosheets (CNs) for high-performance artificial photosynthesis of H_2O_2. Notably, this typical Z-scheme photocatalyst exhibits the highest H_2O_2 generation rate of 732.4 μmol g^{-1} h^{-1}, higher than that of individual catalysts, even maintaining 140.5 μmol g^{-1} h^{-1} under broad-spectrum response irradiation (λ > 700 nm). From the analysis of experimental characterization and density functional theory calculations, the superior performance of CN/WO heterostructures is ascribed to an intense localized surface plasmon resonance absorption, appropriate band alignment, and strong internal electric field. This work not only elucidates the key role of chemically bonded and plasmonic heterostructures but also paves an avenue for the rational design and construction of Z-scheme photocatalysts for solar energy conversion.

Introduction

Hydrogen peroxide (H_2O_2) is an efficient, safe, green, and environment friendly oxidant, which is widely used in the papermaking industry, organic synthesis, sewage treatment, and medical and sanitary fields.[1–3] As a renewable energy source, H_2O_2 has progressively gained lot of attention in the past few years.[4] Compared with hydrogen,[5,6] H_2O_2 has a higher level of safety and is easier to transport, paving the way for it to become a high-value green chemical oxidant.[7–10] About 95% of the industrial H_2O_2 production is currently derived from the anthraquinone method, requiring massive energy input, hazardous reactions, low efficiency and severe pollution, and other weaknesses.[11,12] Among various alternative strategies to optimize the production of H_2O_2,[13–15] photocatalytic synthesis of H_2O_2 has gradually become a promising candidate in replacing conventional approaches due to the advantages of requiring solar resource input, environmental friendliness, and mild reaction conditions.[16,17] Thus, artificial photosynthesis of H_2O_2 could be an emerging approach that provides breakthroughs for alleviating energy crises and environmental problems.

Various semiconductor materials have been widely used for photocatalytic H_2O_2 production, such as TiO_2,[18] $BiVO_4$,[19] MOF,[20,21] COF,[22–24] and g-C_3N_4.[25–27] Among them, g-C_3N_4 is an excellent semiconductor material for the photocatalytic synthesis of H_2O_2 due to the advantages of good stability, non-toxicity, convenient preparation, strong adjustability, and suitable band structure.[28,29] However, the low photocatalytic reaction efficiency is generally attributed to the recombination of electron–hole pairs, particularly random charge transfer dramatically.[30,31] To address this issue, there is a potential solution to produce Z-scheme junctions, promoting the transfer and separation of photogenerated electron–hole pairs and extending the charge lifetime.[32–36] For example, Z-scheme photocatalysts with one-dimensional (1D) CdS nanowires and two-dimensional (2D) CoS_2 nanosheets presented an excellent photocatalytic hydrogen-evolution rate of 5.54 mmol g^{-1} h^{-1} and an apparent quantum efficiency of 10.2% at 420 nm.[37] 2D bilayer heterostructures with sulfur-vacancy-confined-in $ZnIn_2S_4$ and WO_3 nanosheets as the Z-scheme material,

[a]State Key Laboratory of Fine Chemicals, Frontiers Science Center for Smart Materials Oriented Chemical Engineering, School of Chemical Engineering, Dalian University of Technology, Dalian 116024, P. R. China. E-mail: jhou@dlut.edu.cn

[b]Laboratory of Materials Modification by Laser, Ion and Electron Beams, Ministry of Education, Dalian University of Technology, Dalian 116024, P. R. China

[c]Center of Artificial Photosynthesis for Solar Fuels, School of Science, Westlake University, Hangzhou 310024, P. R. China

[d]Department of Chemistry, School of Science, Westlake University, Hangzhou 310024, P. R. China

[e]School of Engineering Sciences in Chemistry, Biotechnology and Health, Department of Chemistry, KTH Royal Institute of Technology, 10044 Stockholm, Sweden

† Electronic supplementary information (ESI) available. See DOI: https://doi.org/10.1039/d2ta09122d

‡ T. Shao and Y. Chang contributed equally to this work.

showed a hydrogen evolution activity of 11.09 mmol g^{-1} h^{-1} under visible-light irradiation.[38] Chemically bonded α-Fe_2O_3/Bi_4MO_8Cl dot-on-plate Z-scheme junctions exhibited high-performance photocatalytic activity for the selective valorization of aromatic alcohols to aldehydes.[39] Especially, the Z-scheme photocatalytic system of g-C_3N_4 and WO_3 can optimize the photocatalytic performance upon hydrogen production, CO_2 reduction, and photo-degradation owing to the efficient Z-scheme interfacial charge transfer.[40–42] However, the synthesis of the Z-scheme catalyst still limits the charge transfer and separation and photocatalytic applications. Inspired by these points, it is obligatory to develop a Z-scheme material model for the artificial photosynthesis of hydrogen peroxide.

Herein, we develop a chemically bonded and plasmonic Z-scheme junction as a model material by the *in situ* assembly of 1D nonstoichiometric $W_{18}O_{49}$ (WO) onto 2D carbon nitride nanosheets (CN) for high-performance artificial photosynthesis of H_2O_2. As a result, this typical Z-scheme photocatalyst exhibits the highest H_2O_2 generation rate of 732.4 μmol g^{-1} h^{-1}, higher than that of individual catalysts, even maintaining 140.5 μmol g^{-1} h^{-1} under broad-spectrum response irradiation (λ > 700 nm). The interfacial W–N bond not only serves as a charge flow highway but also decreases the charge transfer energy barrier. According to the combined analysis of the experimental characterization and density functional theory calculations, the superior performance of CN/WO heterostructures with the proposed mechanism is ascribed to an intense localized surface plasmon resonance absorption, appropriate band alignment, and strong internal electric field.

Results and discussion

The Z-scheme CN/WO heterostructures, as shown in Scheme 1, can be proposed by the analysis of band gap structures (Fig. S1–S4†) and the relative reports.[40–43] CN/WO heterostructures are synthesized by *in situ* assembly method (Fig. 1a). In brief, firstly, g-C_3N_4 nanosheets were obtained by the conventional calcination and subsequent, sonication and recalcination treatments. The CN was then dispersed in ethanol containing WO precursor by the solvothermal process, leading to the generation of CN/WO-*X* (*X* is the mass ratio of WO).

Scanning electron microscopy (SEM) and transmission electron microscopy (TEM) were applied to characterize the morphology of the heterostructures. TEM image of CN/WO-12.5% (Fig. 1b) indicated the homogeneous coupling of the CN and WO, showing the 1D nanowires on the surface of 2D nanosheets, indicating the successful construction of the CN/WO heterostructure, in agreement with the results of SEM and TEM images (Fig. S5–S7†). In high-resolution transmission electron microscopy (HRTEM), the (010) crystal plane of WO can be seen more clearly on the exposed CN with an average crystal plane spacing of 0.380 nm (Fig. 1c).[44,45] Combined with the HRTEM image of a single WO nanowire (Fig. 1d), these TEM images indicate that WO was grown on CN along the (010) direction, indicating an effective build-up of the CN/WO heterostructures.[43] The energy-dispersive spectra (EDS) of CN/WO-12.5% demonstrated (Fig. S8 and S9†) that the system only contains four elements of C, N, W, and O. The element mapping of CN/WO-12.5% heterostructure illustrates that W and O are uniformly scattered on the CN nanosheets (Fig. 1e–i).

The crystallographic characteristics and phase compositions of the CN/WO heterostructure were characterized by an X-ray diffraction (XRD) pattern (Fig. 2a). The primordial CN exhibits two prominent XRD characteristic diffraction peaks at 2θ = 13.1° and 27.3°, which are assigned to the (100) and (002) planes, representing the in-plane structural filling of tri-*s*-triazine units and interlayer superimposition, respectively.[46,47] The XRD peaks of WO can be indexed to the monoclinic crystal system (JCPDS No. 71-2450).[44] The characteristic diffraction peaks of both WO and CN appear in the heterostructure materials. With the gradual increase of WO, the intensity of the corresponding diffraction peaks increases, while the characteristic peaks intensity of CN decreases, indicating that the WO phase is introduced into the CN phase. Fourier transform

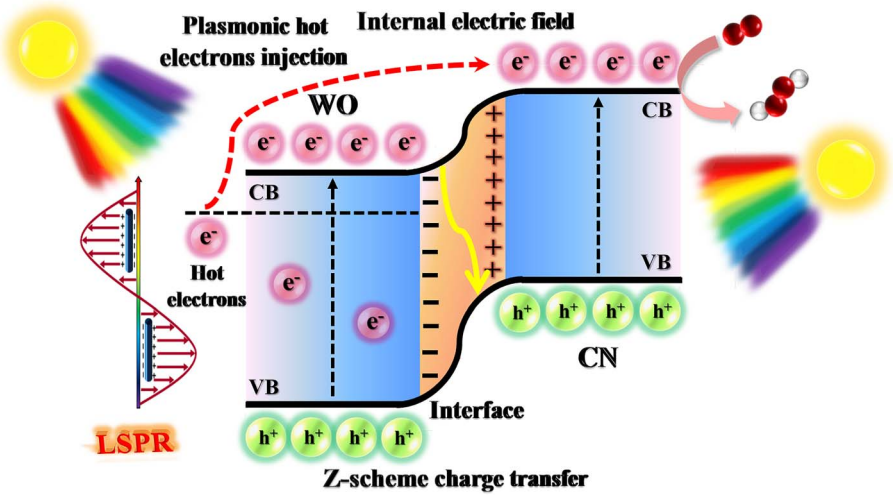

Scheme 1 Illustration of the CN/WO heterostructure for photocatalytic H_2O_2 production.

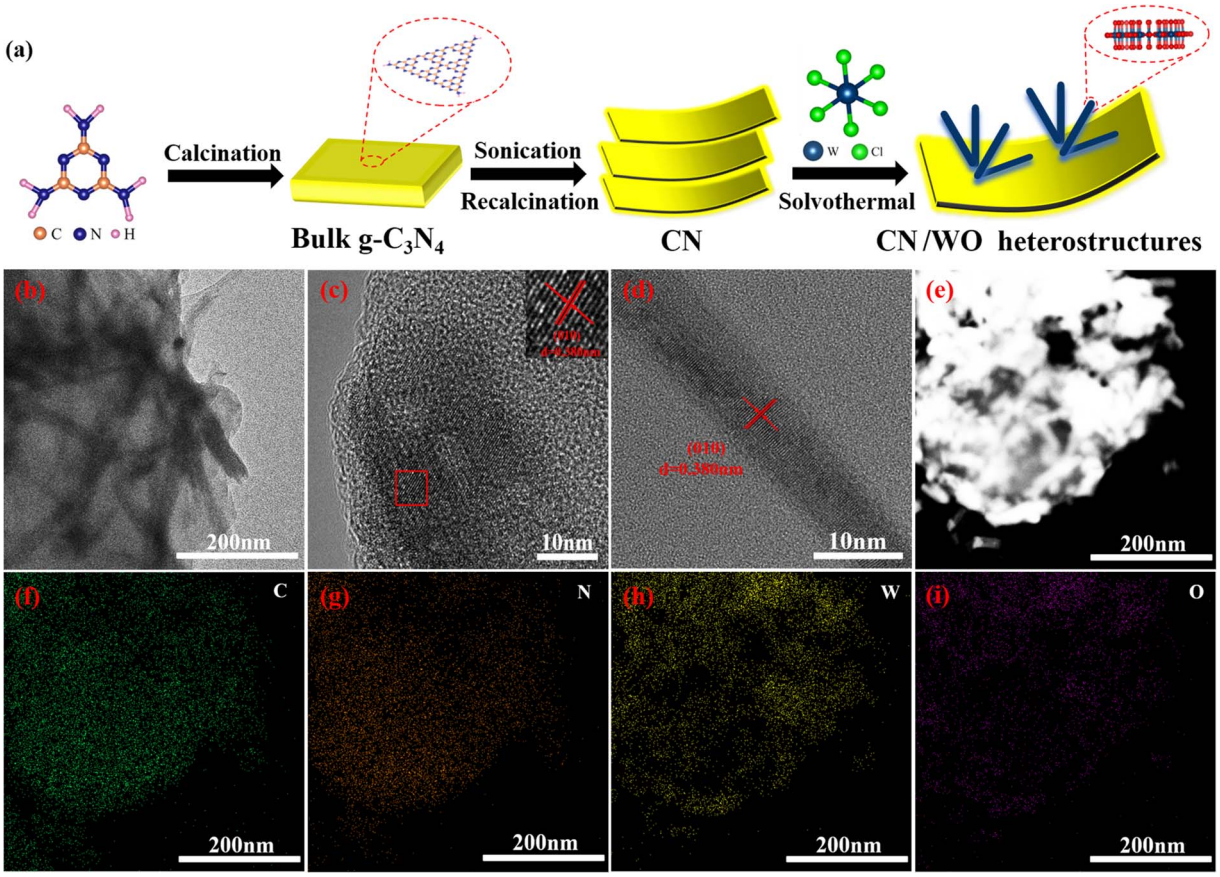

Fig. 1 Morphology analysis. (a) Diagram representation of CN/WO heterostructures synthesis. (b) TEM image and (c) HRTEM image of CN/WO-12.5% heterostructure. (d) HRTEM image of WO nanowire. (e–i) Element mapping of CN/WO-12.5% heterostructure.

infrared (FT-IR) spectra further revealed the molecular structure of CN/WO heterostructures (Fig. 2b). CN shows a peak at around 810 cm^{-1}. While the region of the peak located at 900–1800 cm^{-1} is attributed to the stretching vibrations of aromatic C–N heterocycles, and broad peaks in the range of 3000–3400 cm^{-1} correspond to the stretching vibrations of N–H.[47] The typical stretching vibration bands of 500–1000 cm^{-1} in the FT-IR of WO are assigned to W=O and O–W–O.[48,49] In the CN/WO, the characteristic FT-IR peaks indicate the tight bonding of the two materials. The light absorption capacity of the CN, WO, and CN/WO (Fig. 2c) was revealed by UV-visible diffuse reflectance spectra (UV-vis DRS). The characteristic absorption edge of pristine CN was roughly 468 nm, while the introduction of WO greatly enhanced the light absorption of the catalyst, especially in the visible light region, and the light absorption range of the heterostructures intensified after 450 nm. An intense localized surface plasmon resonance (LSPR) absorption was triggered by the interference of charge oscillations caused by the excitation of electrons from vacancies in the lattice due to the abundance of oxygen vacancies in WO, achieving an enhancement of the light absorption capacity, and thus providing the possibility of the enhanced catalyst activity.[43]

The surface elemental composition and chemical states of the samples were evaluated by X-ray photoelectron spectroscopy (XPS). The full XPS spectrum of CN/WO-12.5% revealed the presence of four elements C, N, W, and O (Fig. S10†). The XPS C 1s spectra of pure CN and CN/WO-12.5% were identical (Fig. 2d), including three peaks situated at 288.5, 286.6, and 284.8 eV, respectively, assigned to N=C–N of sp^2 orbital hybridization, C–NH_x at the edge of the heptazine ring, and C–C introduced externally of sp^2 orbital hybridization.[50,51] The 398.9, 400.1, and 401.2 eV of XPS N 1s spectra of CN are attributed to C–N=C, N–(C_3), and C–N–H, respectively.[52] Simultaneously, a new characteristic peak of 398.0 eV was formed in the CN/WO heterostructure, assigned to the interfacial chemical bonding *via* the W–N bonds between WO and CN (Fig. 2e).[53] The two cleavage orbitals $4f_{7/2}$ and $4f_{5/2}$ of W 4f are presented in pure WO, and two doublets of 35.3 and 37.4 eV belonging to $4f_{7/2}$ and $4f_{5/2}$ of W^{6+}, respectively, while the two doublets of 34.2 and 36.5 eV are assigned to $4f_{7/2}$ and $4f_{5/2}$ of W^{5+} (Fig. 2f), respectively.[43,49] The O 1s spectra of 530.2, 531.2, and 532.9 eV in WO are attributed to the lattice oxygen, oxygen vacancies, and the adsorbed water molecules, respectively.[54]

After assembling CN nanosheets with WO, the characteristic peak of N 1s shifts 0.2 eV toward a low binding energy, while the binding energies of both W^{6+} and W^{5+} are slightly higher than that of pure WO, meanwhile, the characteristic peak of O 1s also shifts slightly toward the higher binding energy. This shift indicates that electron transfer occurs at the CN/WO heterostructure interface, driving the electron flow from WO to CN,

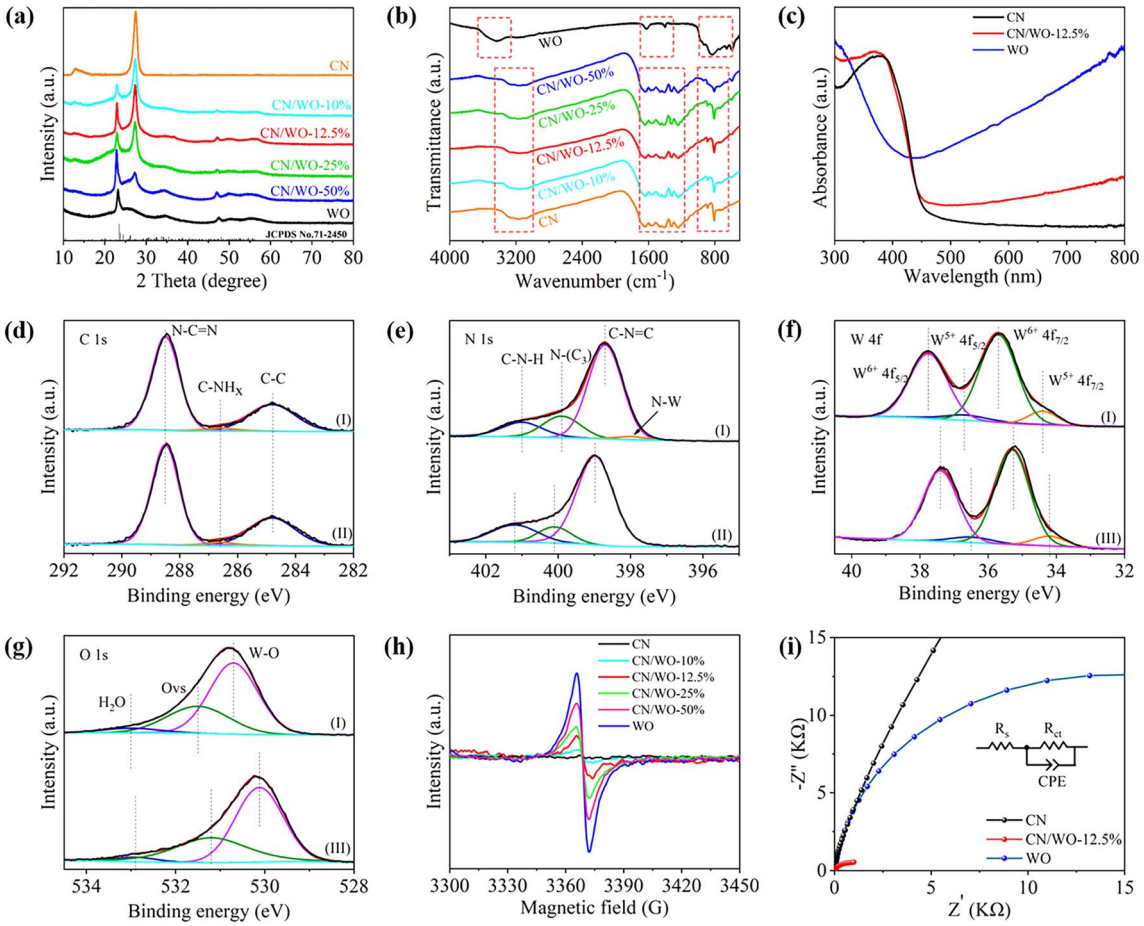

Fig. 2 Structure characterization. (a) XRD pattern of experimental CN/WO heterostructures. (b) FT-IR spectra of CN/WO heterostructures. (c) UV-vis DRS of CN, WO, and CN/WO-12.5% heterostructure. High-resolution XPS spectra of C 1s (d), N 1s (e), W 4f (f), and O 1s (g) for (I) CN/WO-12.5%, (II) CN, (III) WO. (h) EPR spectra of CN/WO heterostructures. (i) Electrochemical impedance spectra of CN, WO, and CN/WO-12.5% heterostructure.

resulting in a decrease in the electron cloud density and a weakened electron shielding effect of the WO component.[43] Electron paramagnetic resonance (EPR) spectroscopy was utilized to detect the presence of oxygen vacancies (Fig. 2h). All catalysts except pure CN showed strong EPR signals, demonstrating the existence of abundant oxygen vacancies in the catalyst. The number of oxygen vacancies in the heterostructures could be effectively regulated by the regulation of the ratio of WO. Photoelectrochemical (PEC) tests of different catalysts also explored the ability of charge separation.[55] Compared with CN and WO, CN/WO-12.5% exhibited a highly superior photocurrent density, proving the efficient separation and migration in the heterostructure (Fig. S11†). Electrochemical impedance spectra (EIS) curves were collected to elucidate the interfacial kinetics of CN, WO, and CN/WO-12.5% (Fig. 2i). The charge transfer resistance of CN/WO-12.5% was significantly lower than that of CN and WO, indicating a significantly-enhanced conductivity and better charge transfer kinetics.

Transient absorption (TA) spectroscopy was used to further investigate the kinetic behavior of the photogenerated charge carriers, especially the photoinduced charge separation at semiconductor interfaces.[38,56] The intuitive pseudo-color TA spectra of CN and CN/WO-12.5% were recorded (Fig. 3a and d). With 500–775 nm as the detection wavelength of the probe, both CN and CN/WO-12.5% exhibited positive TA signals (Fig. 3b and e), which indicate that photogenerated charge recombination occurred at the interface of CN and WO, while a decrease in TA intensity could be observed for both catalysts as the detection time progressed, signifying a decrease in the number of active charges in the photocatalyst.[38] However, the signal intensity of CN/WO-12.5% is lower than that of CN, which revealed that a large amount of charge transfer occurs at the interface of the Z-scheme. As shown in Fig. 3c and f, the delay decay kinetics of different probe wavelengths were used to investigate the surface charge lifetimes of CN and CN/WO-12.5%. The fitted kinetic curves at 600 nm are given in Table S2.† Significantly, the average lifetime of CN/WO-12.5% is clearly longer than that of CN, proving the enhanced charge separation efficiency of CN/WO-12.5%. The recombination of the photogenerated carriers at the W–N bond interfaces was inhibited, thereby increasing the probability of the electron

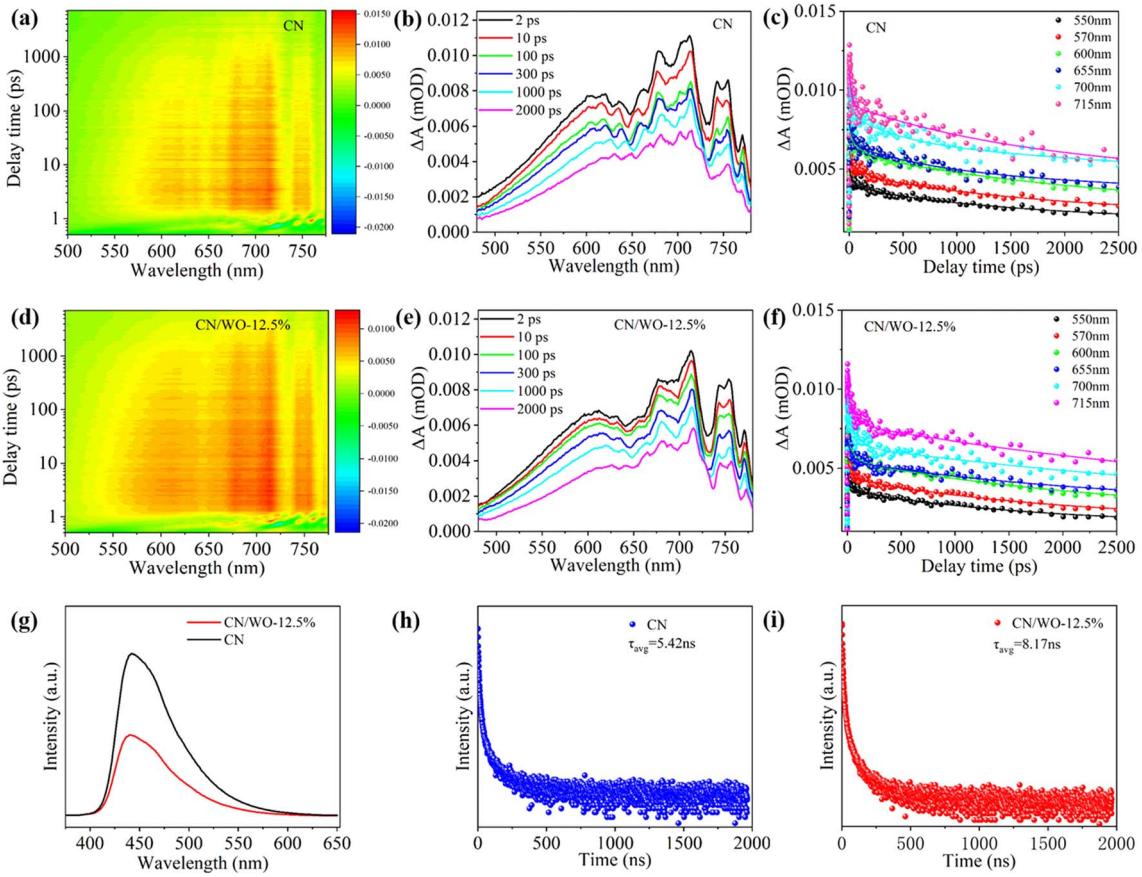

Fig. 3 Kinetic analysis. Pseudo-color fs-TA spectra of (a) CN and (d) CN/WO-12.5% (excitation at 400 nm). Transient fs-TA spectra of (b) CN and (e) CN/WO-12.5% under various probe delays. TA kinetics plots and typical fitting curves of (c) CN and (f) CN/WO-12.5% probed at different probe wavelengths. (g) Steady-state PL spectra of CN and CN/WO-12.5%. Time-resolved PL spectra of (h) CN and (i) CN/WO-12.5%.

participation in the reaction.[56] These results are consistent with time-resolved transient photoluminescence (TRPL) spectra and steady-state photoluminescence (PL) spectra (Fig. 3g), which indicate that the Z-scheme mechanism improves the charge separation efficiency. Meanwhile, the analysis from the biexponential kinetics fitting of PL (Fig. 3h and i and Table S1†) further reveals that the average lifetime of CN/WO-12.5% (τ_{avg} = 8.17 ns) is higher than that of CN (τ_{avg} = 5.42 ns). The combination of the valence band (VB) of WO and the conduction band (CB) of CN in the Z-scheme junction can occur between the photogenerated electrons and holes, suppressing the direct compounding of electrons and holes in CN and enhancing the carrier separation efficiency, thus contributing to the high efficient photocatalytic synthesis of H_2O_2.

To evaluate the performance of photocatalytic O_2 reduction to produce H_2O_2, the photocatalytic tests were performed using various heterostructures under the controllable conditions of variable environmental factors. Meanwhile, a standard curve was established to determine the concentration of H_2O_2 by the traditional cerium sulfate method (Fig. S12†).[21] Under visible-light irradiation (λ > 420 nm), the photocatalytic reaction was saturated with oxygen and water containing 10% isopropanol in volume fraction for 4 hours, and all the photocatalysts exhibited the enhanced H_2O_2 production performance (Fig. 4a). CN/WO-12.5% presented the highest H_2O_2 yield of 732.4 μmol g^{-1} h^{-1} (Fig. 4b), much higher than that of the pure CN (240.0 μmol g^{-1} h^{-1}) and WO (18.5 μmol g^{-1} h^{-1}). After five times of photocatalytic cycle tests, CN/WO-12.5% still showed stable and efficient catalytic performance (Fig. S13†). As shown in Fig. 4b, the average yield of CN/WO-12.5% (562.5 μmol g^{-1} h^{-1}) was 3.75 times that of CN (150.0 μmol g^{-1} h^{-1}) and 22.5 times that of WO (25.0 μmol g^{-1} h^{-1}) under 4 hours of visible-light irradiation. To explore the role of O_2, the photocatalytic H_2O_2 production by CN/WO-12.5% under different atmosphere conditions was studied (Fig. 4c). Under the condition of N_2, no product was detected, while CN/WO-12.5% still showed a certain photocatalytic performance (198.8 μmol g^{-1} h^{-1}) under air atmosphere because O_2 in the air could provide reactants for it. These results imply that H_2O_2 was produced by O_2 reduction rather than by the oxidation of H_2O by photogenerated holes. Fig. 4d reveals the influence of different light intensities on the reaction. The condition of 100 mW cm^{-2} has the best catalytic performance, which may be ascribed to the slow reaction caused by low light intensity, while too high light intensity may lead to partial decomposition of H_2O_2. At the same time, as shown in Fig. 4f, the acid–base conditions of the reaction were

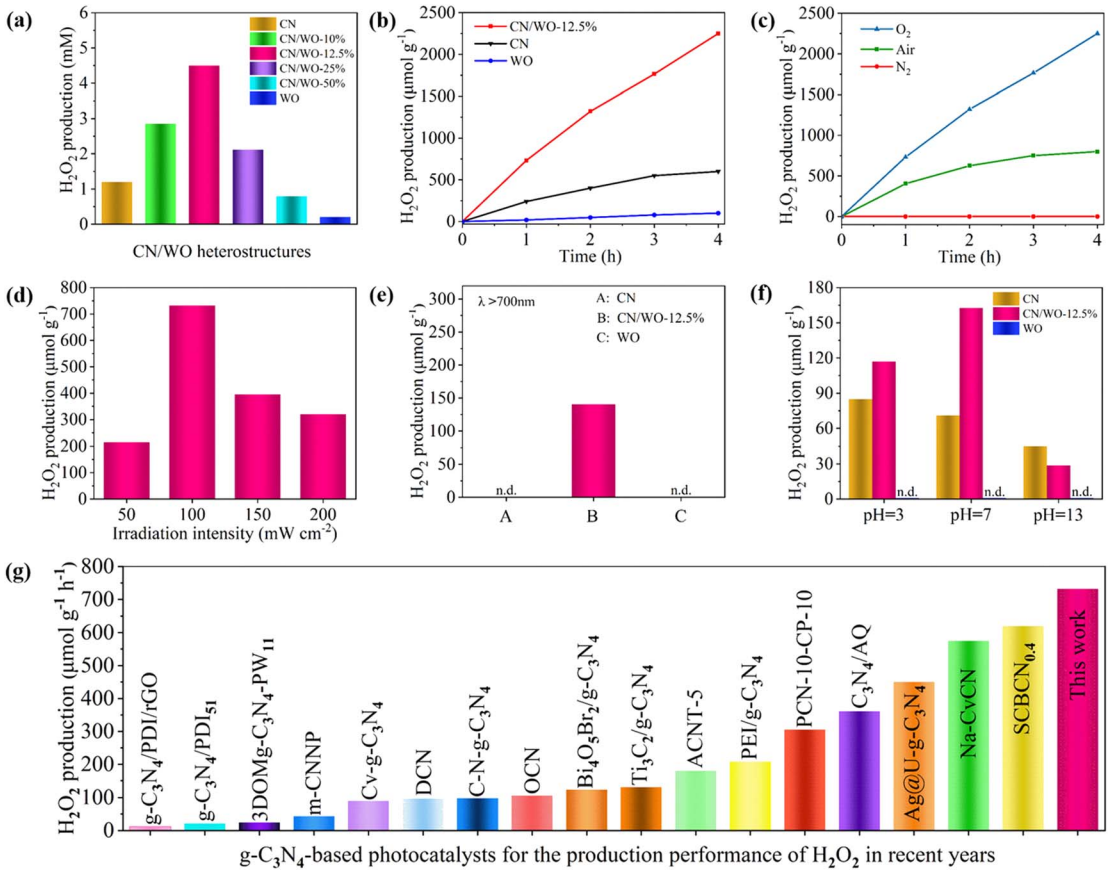

Fig. 4 Performance characterization. (a) H_2O_2 production of CN/WO heterostructures under visible light irradiation (λ > 420 nm). (b) Time course of H_2O_2 production of CN, WO, and CN/WO-12.5% for 4 h. (c) Time course of H_2O_2 production of CN/WO-12.5% under different atmospheric conditions. (d) H_2O_2 production of CN/WO-12.5% at different light intensities for 1 h. (e) H_2O_2 production of CN/WO-12.5% under visible light irradiation (λ > 700 nm). (f) Photocatalytic H_2O_2 production of CN, WO, and CN/WO-12.5% under pH = 3, 7 and 13. (g) H_2O_2 production for g-C_3N_4-based photocatalysts in recent years.

also probed. CN/WO-12.5% showed excellent photocatalytic performance at different pH conditions, with pure water at pH = 7 (162.5 μmol g^{-1} h^{-1}) exceeding pH = 3 (117.1 μmol g^{-1} h^{-1}) and pH = 13 (28.6 μmol g^{-1} h^{-1}). Also, as shown in Fig. S14,† the properties of CN/WO after thorough calcination in the muffle furnace were also investigated. In Fig. 4e, the CN/WO-12.5% heterostructure still showed certain artificial photosynthesis of H_2O_2 capacity (140.5 μmol g^{-1} h^{-1}) under the irradiation (>700 nm), while, remarkably, no products were detected for CN and WO. This is attributed to the LSPR absorption, which leads to the transfer of hot electrons to CN through the chemical bond for O_2 reduction. In contrast, the performance of the artificial photosynthesis of H_2O_2 on CN/WO-12.5% is superior to that on most of the carbon nitride-based catalysts currently reported.[28,52,57–73]

The reaction mechanism of the artificial photosynthesis of H_2O_2 was further investigated. Firstly, EPR was used to detect the reaction intermediate superoxide radicals ($^{\bullet}O_2^-$) with the use of 5,5-dimethyl-1-pyrroline *N*-oxide (DMPO) as the capture agent in methanol solution (Fig. 5a).[38] The test indicates that no signals were detected in either CN or CN/WO-12.5% under the condition of no visible light, indicating that $^{\bullet}O_2^-$ cannot be generated in the system in the dark. After 5 minutes of visible light, both CN and CN/WO-12.5% showed strong signals, which, the CN/WO-12.5% signal was much stronger than that of CN, thus, proving that the H_2O_2 production in this system is a sequential two-electron reduction ($O_2 \rightarrow {}^{\bullet}O_2^- \rightarrow H_2O_2$), rather than the one-step reduction ($O_2 \rightarrow H_2O_2$). The possible mechanism of the photocatalytic oxygen reduction for the H_2O_2 production of CN/WO heterostructures is shown in Fig. 5b. In the Z-scheme heterostructure with chemical bond, the light-trapping ability of the system was enhanced by benefiting from the LSPR absorption. The CB electrons of WO could recombine directly with the holes on the VB of CN to the effect of the internal electric field. Hot electrons generated on WO excited by LSPR can be continuously injected into CN through the W–N bond, which electrons (including hot electrons) on CN accomplish the efficient catalytic activity. Meanwhile, after the catalytic reaction, the morphology and structure of CN/WO-12.5% did not significantly change (Fig. S15–S18†), indicating the structural stability of the photocatalyst, which provided the necessary conditions for the artificial photosynthesis of H_2O_2.

Density functional theory (DFT) calculations were used to further probe the thermodynamics and dynamics of the CN/WO

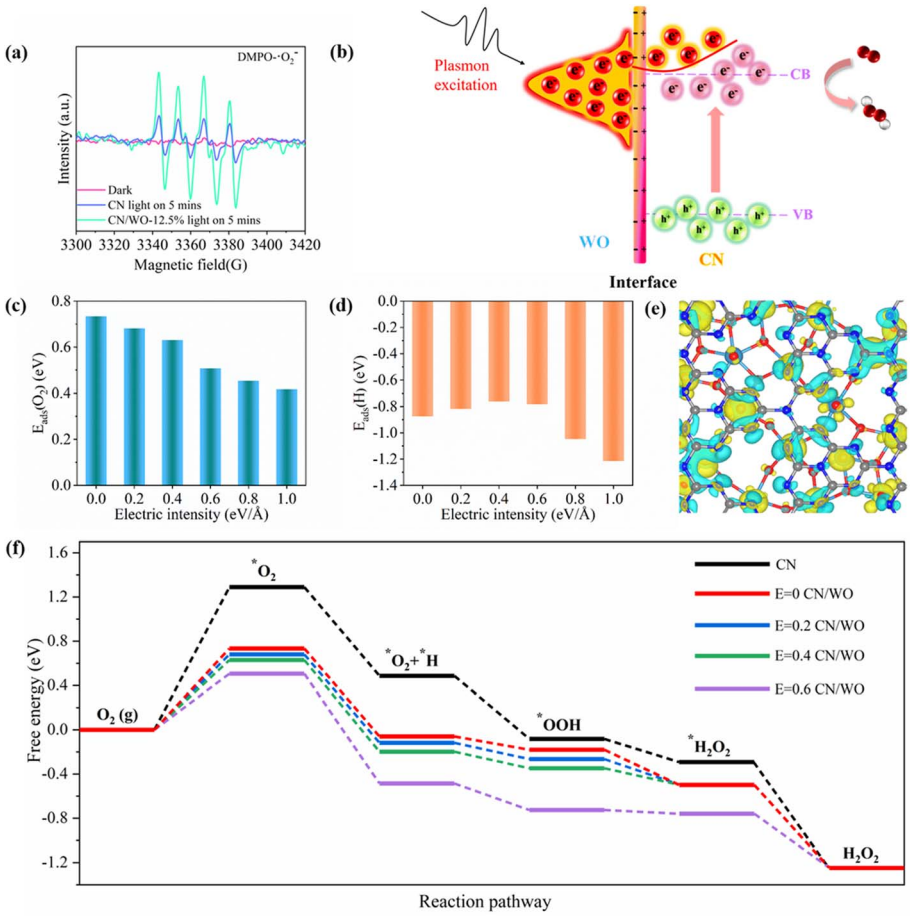

Fig. 5 Mechanism analysis. (a) EPR signals of $^{\cdot}O_2^-$ over CN and CN/WO-12.5% (DMPO in methanol). (b) Possible mechanism of artificial photosynthesis of H_2O_2 of CN/WO heterostructures. Adsorption energies of (c) O_2 and (d) H under different simulated electric fields on CN/WO heterostructures. (e) Charge density difference of CN/WO heterostructures. Yellow and blue indicate electron accumulation and depletion, respectively. (f) Free energy profiles for photocatalytic H_2O_2 performance of pristine CN and CN/WO heterostructures under different electric fields.

heterostructures (Fig. S19 and Tables S3–S9†). Numerous previous studies have shown that the local electric field of plasma semiconductors tends to be enhanced under LSPR absorption.[43,74] Therefore, we applied an incremental electric field along the negative direction of the *Z*-axis to simulate the photogenerated electric potential during the catalytic process. In the $2e^-$ ORR hydrogen peroxide production reaction, the rate-determining step is the formation of *OOH, for which the adsorption of O_2 and H is the critical prerequisite.[75] The adsorption sites of O_2 and H at the pure CN and CN/WO heterostructures were analyzed (Fig. S20 and S21†), meanwhile, the adsorption energies of O_2 (Fig. 5c) and H (Fig. 5d) corresponding to the CN/WO heterostructures under different simulated electric field strengths were given separately. The changes in adsorption energies of O_2 revealed that the adsorption of O_2 was significantly intensified. Whereas, the variations of adsorption energies of H point to the adsorption of H firstly weaker until the electric intensity of 0.6 eV $Å^{-1}$, then turns to augmented, revealing that the local electric field generated by LSPR can indeed increase the adsorption of O_2 and H, which is conducive to the formation of *OOH. At the same time, in Fig. 5e, the charge difference density of CN/WO heterostructures was calculated by kinetics, with more significant charge redistribution between CN and WO, the electron bias toward the CN side that favored the $2e^-$ ORR reaction, consistent with our experimental results. The Gibbs free energy (ΔG) of the reaction step (Fig. 5f), and the $2e^-$ ORR free energy for each species were calculated and are shown in Tables S3–S9.† When there was no simulated electric field, both $*O_2$ and *H in CN/WO were far lower than pure CN, which indicated that the Z-scheme junction is favorable for the *OOH formation. This in turn reflects that the $2e^-$ ORR performance of the CN/WO is thermodynamically superior to that of CN. After increasing the simulated electric field, the energy barrier of the intermediate decreases, which indicated that the enhanced local electric field means the concentration of plasma, generating high-energy hot electrons on the surface of WO, which can then be directly injected into CN, thus, contributing to $2e^-$ ORR activity. It is worth noting that the appropriate electric field within 0–0.6eV $Å^{-1}$ is beneficial to the catalytic process. Whereas, in an oversized electric field such as 0.8 eV $Å^{-1}$ or 1 eV $Å^{-1}$, the energy barrier of *OOH will be lower than that of $*H_2O_2$, and the process from *OOH to

*H_2O_2 will pose difficulties leading to unfavorable photosynthesis of H_2O_2.

Conclusions

In summary, a chemically bonded and plasmonic Z-scheme junction has been developed for high-performance artificial photosynthesis of H_2O_2 by the *in situ* assembly of plasmonic WO onto two-dimensional carbon nitride nanosheets. The typical Z-scheme photocatalyst exhibits an intriguing H_2O_2 generation rate of 732.4 μmol g^{-1} h^{-1}, even maintaining 140.5 μmol g^{-1} h^{-1} under broad-spectrum response irradiation (λ > 700 nm). Based on detailed experimental characterization and DFT calculations, LSPR greatly promotes light trapping and enhances the adsorption of oxygen. Attributed to the Z-scheme mechanism by the internal electric field with a W–N bond, it significantly boosts carrier separation and transfer, while electrons can be continuously transferred to CN through chemical bonding, fostering an efficient photocatalytic activity. This work not only elucidates the key role of chemically bonded and plasmonic heterostructures but also provides an avenue for the rational design and construction of Z-scheme photocatalysts for solar energy conversion.

Conflicts of interest

The authors declare no conflicts of interest.

Acknowledgements

This work was supported by the National Natural Science Foundation of China (No. 21972015, 22088102), the Young top talents project of Liaoning Province (No. XLYC1907147), the Fundamental Research Funds for the Central Universities (No. DUT22QN207, DUT22LAB602, DUT2022TB05), the Liaoning Revitalization Talent Program (No. XLYC2008032) and Special Project for Key Research and Development Program of Xinjiang Autonomous Region (No. 2022B01033-3).

Notes and references

1 Y. Sun, L. Han and P. Strasser, *Chem. Soc. Rev.*, 2020, **49**, 6605–6631.
2 Y. Shiraishi, T. Takii, T. Hagi, S. Mori, Y. Kofuji, Y. Kitagawa, S. Tanaka, S. Ichikawa and T. Hirai, *Nat. Mater.*, 2019, **18**, 985–993.
3 L. Fu, C. Qi, J. Lin and P. Huang, *Chem. Soc. Rev.*, 2018, **47**, 6454–6472.
4 Z. Lu, G. X. Chen, S. Siahrostami, Z. Chen, K. Liu, J. Xie, L. Liao, T. Wu, D. Lin, Y. Liu, T. F. Jaramillo, J. K. Nørskov and Y. Cui, *Nat. Catal.*, 2018, **1**, 156–162.
5 T. Lu, T. Li, D. Shi, J. Sun, H. Pang, L. Xu, J. Yang and Y. Tang, *SmartMat*, 2021, **2**, 591–602.
6 S. Li, W. Xu, L. Meng, W. Tian and L. Li, *Small Sci.*, 2022, **2**, 2100112.
7 Q. Wu, J. Cao, X. Wang, Y. Liu, Y. Zhao, H. Wang, Y. Liu, H. Huang, F. Liao, M. Shao and Z. Kang, *Nat. Commun.*, 2021, **12**, 483.
8 Q. Zhang, X. Tan, N. M. Bedford, Z. Han, L. Thomsen, S. Smith, R. Amal and X. Lu, *Nat. Commun.*, 2020, **11**, 4181.
9 H. Hou, X. Zeng and X. Zhang, *Angew. Chem., Int. Ed.*, 2020, **59**, 17356–17376.
10 S. A. Mousavi Shaegh, N. T. Nguyen, S. M. Mousavi Ehteshami and S. Chan, *Energy Environ. Sci.*, 2012, **5**, 8225–8228.
11 R. J. Lewis, K. Ueura, X. Liu, Y. Fukuta, T. E. Davies, D. J. Morgan, L. Chen, J. Qi, J. Singleton, J. K. Edwards, S. J. Freakley, C. J. Kiely, Y. Yamamoto and G. J. Hutchings, *Science*, 2022, **376**, 615–620.
12 J. K. Edwards, B. Solsona, E. N. Ntainjua, A. F. Carley, A. A. Herzing, C. J. Kiely and G. J. Hutchings, *Science*, 2009, **323**, 1037–1041.
13 Y. Wang, D. Wang and Y. Li, *SmartMat*, 2021, **2**, 56–75.
14 S. J. Freakley, Q. He, J. H. Harrhy, L. Lu, D. A. Crole, D. J. Morgan, E. N. Ntainjua, J. K. Edwards, A. F. Carley, A. Y. Borisevich, C. J. Kiely and G. J. Hutchings, *Science*, 2016, **351**, 965–968.
15 A. Huang, R. S. Delima, Y. Kim, E. W. Lees, F. G. L. Parlane, D. J. Dvorak, M. B. Rooney, R. P. Jansonius, A. G. Fink, Z. Zhang and C. P. Berlinguette, *J. Am. Chem. Soc.*, 2022, **144**, 14548–14554.
16 L. Liu, M. Gao, H. Yang, X. Wang, X. Li and A. I. Cooper, *J. Am. Chem. Soc.*, 2021, **143**, 19287–19293.
17 C. Wu, Z. Teng, C. Yang, F. Chen, H. Yang, L. Wang, H. Xu, B. Liu, G. Zheng and Q. Han, *Adv. Mater.*, 2022, **34**, 2110266.
18 L. Zheng, H. Su, J. Zhang, L. S. Walekar, H. V. Molamahmood, B. Zhou, M. Long and Y. Hu, *Appl. Catal., B*, 2018, **239**, 475–484.
19 H. Hirakawa, S. Shiota, Y. Shiraishi, H. Sakamoto, S. Ichikawa and T. Hirai, *ACS Catal.*, 2016, **6**, 4976–4982.
20 Y. Isaka, Y. Kawase, Y. Kuwahar, K. Mor and H. Yamashita, *Angew. Chem., Int. Ed.*, 2019, **58**, 5402–5406.
21 Y. Hao, L. Chen, J. Li, Y. Guo, X. Su, M. Shu, Q. Zhang, W. Gao, S. Li, Z. Yu, L. Gu, X. Feng, A. Yin, R. Si, Y. Zhang, B. Wang and C. Yan, *Nat. Commun.*, 2021, **12**, 2682.
22 H. Wang, C. Yang, F. Chen, G. Zheng and Q. Han, *Angew. Chem., Int. Ed.*, 2022, **61**, e202202328.
23 W. Zhao, P. Yan, B. Li, M. Bahri, L. Liu, X. Zhou, R. Clowes, N. D. Browning, Y. Wu, J. W. Ward and A. I. Cooper, *J. Am. Chem. Soc.*, 2022, **144**, 9902–9909.
24 M. Kou, Y. Wang, Y. Xu, L. Ye, Y. Huang, B. Jia, H. Li, J. Ren, Y. Deng, J. Chen, Y. Zhou, K. Lei, L. Wang, W. Liu, H. Huang and T. Ma, *Angew. Chem., Int. Ed.*, 2022, **61**, e202200413.
25 G. Moon, M. Fujitsuka, S. Kim, T. Majima, X. Wang and W. Choi, *ACS Catal.*, 2017, **7**, 2886–2895.
26 H. Ou, P. Yang, L. Lin, M. Anpo and X. Wang, *Angew. Chem., Int. Ed.*, 2017, **56**, 10905–10910.
27 H. Ou, C. Tang, X. Chen, M. Zhou and X. Wang, *ACS Catal.*, 2019, **9**, 2949–2955.
28 J. Cai, J. Huang, S. Wang, J. Iocozzia, Z. Sun, J. Sun, Y. Yang, Y. Lai and Z. Lin, *Adv. Mater.*, 2019, **31**, 1806314.

29 B. Zhu, B. Cheng, J. Fan, W. Ho and J. Yu, *Small Struct.*, 2021, **2**, 2100086.
30 L. Su, P. Wang, X. Ma, J. Wang and S. Zhan, *Angew. Chem., Int. Ed.*, 2021, **60**, 21261–21266.
31 N. Wang, K. Yao, A. Vomiero, Y. Wang and H. Liang, *SmartMat*, 2021, **2**, 423–425.
32 Y. Zhang, L. Ran, Z. Li, P. Zhai, B. Zhang, Z. Fan, C. Wang, X. Zhang, J. Hou and L. Sun, *Trans. Tianjin Univ.*, 2021, **27**, 348–357.
33 S. Chen, J. J. M. Vequizo, Z. Pan, T. Hisatomi, M. Nakabayashi, L. Lin, Z. Wang, K. Kato, A. Yamakata, N. Shibata, T. Takata, T. Yamada and K. Domen, *J. Am. Chem. Soc.*, 2021, **143**, 10633–10641.
34 Y. Zhang, D. Yao, B. Xia, H. Xu, Y. Tang, K. Davey, J. Ran and S. Qiao, *Small Sci.*, 2021, **2**, 2000052.
35 C. Zeng, Y. Hu, T. Zhang, F. Dong, Y. Zhang and H. Huang, *J. Mater. Chem. A*, 2018, **6**, 16932–16942.
36 X. Zhang, Y. Wei and R. Yu, *Small Struct.*, 2022, **3**, 2100130.
37 P. Wang, Y. Mao, L. Li, Z. Shen, X. Luo, K. Wu, P. An, H. Wang, L. Su, Y. Li and S. Zhan, *Angew. Chem., Int. Ed.*, 2019, **58**, 11329–11334.
38 Z. Li, J. Hou, B. Zhang, S. Cao, Y. Wu, Z. Gao, X. Nie and L. Sun, *Nano Energy*, 2019, **59**, 537–544.
39 Z. Zhu, H. Huang, L. Liu, F. Chen, N. Tian, Y. Zhang and H. Yu, *Angew. Chem., Int. Ed.*, 2022, **61**, e202203519.
40 W. Yu, J. Chen, T. Shang, L. Chen, L. Gu and T. Peng, *Appl. Catal., B*, 2017, **219**, 693–704.
41 X. Li, X. Song, C. Ma, Y. Cheng, D. Shen, S. Zhang, W. Liu, P. Huo and H. Wang, *ACS Appl. Nano Mater.*, 2020, **3**, 1298–1306.
42 T. Xiao, Z. Tang, Y. Yang, L. Tang, Y. Zhou and Z. Zou, *Appl. Catal., B*, 2018, **220**, 417–428.
43 Z. Zhang, J. Huang, Y. Fang, M. Zhang, K. Liu and B. Dong, *Adv. Mater.*, 2017, **29**, 1606688.
44 N. Zhang, A. Jalil, D. Wu, S. Chen, Y. Liu, C. Gao, W. Ye, Z. Qi, H. Ju, C. Wang, X. Wu, L. Song, J. Zhu and Y. Xiong, *J. Am. Chem. Soc.*, 2018, **140**, 9434–9443.
45 H. Zhang, Y. Wang, S. Zuo, W. Zhou, J. Zhang and X. Lou, *J. Am. Chem. Soc.*, 2021, **143**, 2173–2177.
46 D. Zhao, Y. Wang, C. Dong, Y. Huang, J. Chen, F. Xue, S. Shen and L. Guo, *Nat. Energy*, 2021, **6**, 388–397.
47 D. Zhao, C. Dong, B. Wang, C. Chen, Y. Huang, Z. Diao, S. Li, L. Guo and S. Shen, *Adv. Mater.*, 2019, **31**, 1903545.
48 J. Polleux, N. Pinna, M. Antonietti and M. Niederberger, *J. Am. Chem. Soc.*, 2005, **127**, 15595–15601.
49 G. Xi, S. Ouyang, P. Li, J. Ye, Q. Ma, N. Su, H. Bai and C. Wang, *Angew. Chem., Int. Ed.*, 2012, **51**, 2395–2399.
50 H. Yu, R. Shi, Y. Zhao, T. Bian, Y. Zhao, C. Zhou, G. I. N. Waterhouse, L. Wu, C. Tung and T. Zhang, *Adv. Mater.*, 2017, **29**, 1605148.
51 Y. Wang, P. Du, H. Pan, L. Fu, Y. Zhang, J. Chen, Y. Du, N. Tang and G. Liu, *Adv. Mater.*, 2019, **31**, 1807540.
52 W. Liu, C. Song, M. Kou, Y. Wang, Y. Deng, T. Shimada and L. Ye, *Chem. Eng. J.*, 2021, **425**, 130615.
53 R. Shen, L. Zhang, N. Li, Z. Lou, T. Ma, P. Zhang, Y. Li and X. Li, *ACS Catal.*, 2022, **12**, 9994–10003.
54 Z. Wei, W. Wang, W. Li, X. Bai, J. Zhao, E. C. M. Tse, D. L. Phillips and Y. Zhu, *Angew. Chem., Int. Ed.*, 2021, **60**, 8236–8242.
55 X. Zhang, P. Zhai, Y. Zhang, Y. Wu, C. Wang, L. Ran, J. Gao, Z. Li, B. Zhang, Z. Fan, L. Sun and J. Hou, *J. Am. Chem. Soc.*, 2021, **143**, 20657–20669.
56 L. Ran, Z. Li, B. Ran, J. Cao, Y. Zhao, T. Shao, Y. Song, M. K. H. Leung, L. Sun and J. Hou, *J. Am. Chem. Soc.*, 2022, **144**, 17097–17109.
57 Y. Shiraishi, S. Kanazawa, Y. Kofuji, H. Sakamoto, S. Ichikawa, S. Tanaka and T. Hirai, *Angew. Chem., Int. Ed.*, 2014, **53**, 13454–13459.
58 S. Li, G. Dong, R. Hailili, L. Yang, Y. Li, F. Wang, Y. Zeng and C. Wang, *Appl. Catal., B*, 2016, **190**, 26–35.
59 Y. Kofuji, Y. Isobe, Y. Shiraishi, H. Sakamoto, S. Tanaka, S. Ichikawa and T. Hirai, *J. Am. Chem. Soc.*, 2016, **138**, 10019–10025.
60 S. Zhao, X. Zhao, H. Zhang, J. Lia and Y. Zhu, *Nano Energy*, 2017, **35**, 405–414.
61 H. Kim, Y. Choib, S. Hu, W. Y. Choi and J. H. Kim, *Appl. Catal., B*, 2018, **229**, 121–129.
62 Y. Fu, C. Liu, M. Zhang, C. Zhu, H. Li, H. Wang, Y. Song, H. Huang, Y. Liu and Z. Kang, *Adv. Energy Mater.*, 2018, **8**, 1802525.
63 Z. Wei, M. Liu, Z. Zhang, W. Yao, H. Tan and Y. Zhu, *Energy Environ. Sci.*, 2018, **11**, 2581–2589.
64 L. Shi, L. Yang, W. Zhou, Y. Liu, L. Yin, X. Hai, H. Song and J. Ye, *Small*, 2018, **14**, 1703142.
65 Y. Yang, Z. Zeng, G. Zeng, D. Huang, R. Xiao, C. Zhang, C. Zhou, W. Xiong, W. Wang, M. Cheng, W. Xue, H. Guo, X. Tang and D. He, *Appl. Catal., B*, 2019, **258**, 117956.
66 X. Zhao, Y. You, S. Huang, Y. Wu, Y. Ma, G. Zhang and Z. Zhang, *Appl. Catal., B*, 2020, **278**, 119251.
67 X. Zeng, Y. Liu, Y. Kang, Q. Li, Y. Xia, Y. Zhu, H. Hou, M. H. Uddin, T. R. Gengenbach, D. Xia, C. Sun, D. T. Mccarthy, A. Deletic, J. Yu and X. Zhang, *ACS Catal.*, 2020, **10**, 3697–3706.
68 L. Zhou, J. Lei, F. Wang, L. Wang, M. R. Hoffmann, Y. Liu, S. In and J. Zhang, *Appl. Catal., B*, 2021, **288**, 119993.
69 P. Ma, X. Zhang, C. Wang, Z. Wang, K. Wang, Y. Feng, J. Wang, Y. Zhai, J. Deng, L. Wang and K. Zheng, *Appl. Catal., B*, 2022, **300**, 120736.
70 Q. You, C. Zhang, M. Cao, B. Wang, J. Huang, Y. Wang, S. Deng and G. Yu, *Appl. Catal., B*, 2023, **321**, 121941.
71 L. Chen, S. Li, Z. Yang, C. Chen, C. Chu and B. Chen, *Appl. Catal., B*, 2022, **305**, 121066.
72 Y. Zhu, Y. Sun, J. Khan, H. Liu, G. He, X. Liu, J. Xiao, H. Xie and L. Han, *Chem. Eng. J.*, 2022, **443**, 136501.
73 F. Xue, Y. Si, C. Cheng, W. Fu, X. Chen, S. Shen, L. Wang and M. Liu, *Nano Energy*, 2022, **103**, 107799.
74 X. Jiang, J. Huang, Z. Bi, W. Ni, G. Gurzadyan, Y. Zhu and Z. Zhang, *Adv. Mater.*, 2022, **34**, 2109330.
75 X. Zhang, P. Ma, C. Wang, L. Gan, X. Chen, P. Zhang, Y. Wang, H. Li, L. Wang, X. Zhou and K. Zheng, *Energy Environ. Sci.*, 2022, **15**, 830–842.